Mon. Not. R. astr. Soc. (1982) **199**, 171–196

A stationary and a slowly rotating model of a triaxial elliptical galaxy

Althea Wilkinson and R. A. James *Astronomy Department, University of Manchester, Oxford Road, Manchester M13 9PL*

Received 1981 August 17; in original form 1981 May 27

Summary. Evolving models of a stationary and a slowly rotating triaxial ellipsoidal system are presented. The final large-scale properties of the models are in general promisingly similar to those of observed elliptical galaxies, and there is no suggestion that the triaxial shape disappears over 4×10^9 years. The orbits of 2 per cent of the 25 000 stars have been followed in detail, and these show that essentially only two simple orbital families are involved.

1 Introduction

Recent observations have shown that the old view of elliptical galaxies, as self-gravitating isothermal spheroidal bodies of stars flattened by rotation, is no longer tenable.

Since the first rotation curve of an elliptical galaxy (NGC 4697) was published by Bertola & Capaccioli (1975), the rotation velocities of at least 46 ellipticals and early-type galaxies have become available (for a review, see Bertola 1980: for individual measurements Illingworth 1977; Petersen 1978; Davies 1979; Schechter & Gunn 1979; Capaccioli 1979; Young *et al.* 1978; Efstathiou, Ellis & Carter 1980). In most cases the galaxies are found to rotate too slowly, by a factor of about three, to produce the observed flattening (NGC 3557 and 4697 observed by Davies are counter-examples).

These spectral measurements are also beginning to yield direct information on the line of sight velocity dispersions in these galaxies. As a result, it is clear that the ratio of the peak rotation velocity to the central (maximum) line of sight velocity dispersion, the single dimensionless number which can be taken to characterize the rotation of a galaxy, is usually much lower than the value characterizing the equivalent spheroidal model.

Measurements of rotation about the minor axis, which has been suggested by Contopoulos (1956) as being one of the indications of triaxiality, are still somewhat controversial. The number of possible detections is still small (Bertola & Capaccioli 1980; Schecter & Gunn 1979; Davies 1979).

Information has also been accumulating from detailed photometry (Evans 1951; Liller 1960, 1966; Carter 1978, King 1978, Strom & Strom 1978a, b; Williams & Schwarzschild 1978; Bertola & Galletta 1979; Barbon, Benacchio & Capaccioli 1976) that the ellipticity of the isophotes often changes with radius. This change is typically about one ellipticity class, though there are galaxies (usually with companions) where larger changes are seen, and

equally there are galaxies that have constant ellipticity. Di Tullio (1979) finds that the ellipticity tends to increase outwards for galaxies in clusters or with neighbours, and to increase inwards for isolated galaxies.

Accompanying the ellipticity changes, it has been found that the position angle of the major axis of the isophotes sometimes rotates as a function of distance from the centre (IC 1459, Williams & Schwarzschild 1978, is a counter-example). In most cases (91.7 per cent in the sample of Bennachio & Galletta 1980) this twist is less than 10°, and may therefore be due partly to errors of measurement (thought to be $\leqslant 5°$ in most of the measurements quoted above). However, where twists can be easily distinguished, Galletta (1980) has found that the galaxies with rounder isophotes tend to show larger twists. Since many of these galaxies tend to be in groups or clusters, it is not yet clear whether this effect is an intrinsic property of elliptical galaxies or due to the intervention of neighbouring galaxies.

Theoretically, even before the new observational evidence, Binney (1975, 1976) had predicted that pressure-anisotropy dominated galaxies should be capable of forming and should be the natural outcome of the pancake picture of galaxy formation (Sunyaev & Zeldovich 1972; Lin, Mestel & Shu 1965). He then concluded that the galaxies so formed must be triaxial because there was no reason to suppose that the initial conditions should be axially symmetric, and that deviations from axisymmetry should at least partly survive the relaxation process and be seen in present-day galaxies. Aarseth & Binney (1978) subsequently showed by means of a 500-body model followed for 1/10 of a Hubble time, that triaxial initial conditions were indeed likely to lead to triaxial equilibrium systems, with the shape being maintained by two non-classical integrals.

Since then, Schwarzschild (1979) has built a self-consistent galaxy model by combining the simplest possible orbits of single particles in a triaxial potential. This suggests that probably any reasonable triaxial form will not be disrupted once it has been established.

The problem had also been approached from the rapidly rotating end by Miller (1978) and Miller & Smith (1979, 1981), who followed the evolution of rapidly rotating initially spherical bodies of 100 000 stars for approximately 1/10 of a Hubble time. Such collapses invariably produced stable prolate bars rotating about a short axis, at a speed too great to be comparable with the majority of observed ellipticals. These particular models are perhaps more relevant to bars in spiral galaxies than to the ellipticals themselves.

The main outstanding questions at this point are whether triaxial structures really can persist for a Hubble time, and what the effects of slow rotation might be.

2 The code

The code used in these simulations was the particle-mesh algorithm described by James (1977) and James & Sellwood (1978) with a $33 \times 33 \times 33$ mesh and 25 000 particles. Like those of Hohl (1978) and Miller (1978) this code uses fast Fourier transforms to determine the gravitational potential from the density distribution, but in the version developed by James (1977) substantial storage and time savings have been made by using a boundary charge correction technique.

This code has the advantage of allowing models with a large number of particles to be run for periods comparable with a Hubble time, while maintaining the number of significant bits stored for each quantity of interest (position and velocity) at a level where individual orbits are not noticeably disturbed by random noise.

The chief drawback to the present version of the code is the restricted spatial resolution. It can be calculated that in a real galaxy the time between stellar encounters which are close enough for the stars to form binary pairs is greater than 10^{13} yr, or much longer than the lifetime of a galaxy. For this reason such encounters must be prevented in the model, and the

practical result is that the force law must be tailored so that at close range the forces fall to zero rather than following the true point-mass Newtonian law. This means that the effect on the net field of particles within about two mesh spaces is not accurately represented, and so detail smaller than ~1/16 of the mesh width cannot be reliably resolved. The effect can be reduced to some extent by increasing the number of mesh cells in the cubic mesh or made as small as necessary by using a polar mesh (e.g. van Albada & van Gorkom 1977; van Albada 1980).

The models were run and most of the analysis done on the CDC 7600 computer at the University of Manchester Regional Computer Centre.

3 The models

Two models were set up – a non-rotating model having a triaxial initial geometry (model A) and a similarly shaped but slowly rotating model (model B). Being free from the complications of rotation, model A was intended to provide a standard with which later models could be compared, but it can also be directly compared with those elliptical systems which are known to have very low rotation velocities (zero to within the errors of measurement, see, e.g. Illingworth 1977).

3.1 MODEL A: NON-ROTATING

The parameters of this model, in terms of model units are given in Table 1. The length unit, l = (mesh side in kpc/30) kpc, and the time unit,

$$t = \frac{1}{100}\sqrt{\frac{(\text{system dimensions})^3}{GM}} = 2.1034\times 10^{26}\sqrt{\frac{(\text{system dimensions, kpc})^3}{(\text{system mass, g})}}\ \text{yr},$$

may be scaled to be appropriate to a galactic nucleus or a cluster of galaxies, but for the present purposes, a major axis diameter of 50 kpc, mass of 10^{44} g (typical of a normal elliptical galaxy) and mesh side of 60 kpc yield a time interval of 1.66×10^6 yr. The velocity unit is given by l/t. The equivalent parameters in these galaxy units are given in brackets in Table 1.

The initial shape was chosen to be that which Aarseth & Binney (1978) have shown to be likely to maintain some degree of triaxiality. The other conditions, the uniformly random

Table 1. Model parameters.

Model	A	B
Diameter (major axis)	25 mesh units (50 kpc)	25 mesh units (50 kpc)
Axial ratios	0.15: 0.33: 1.0	0.15: 0.33: 1.0
Particle distribution	Uniform random	Uniform random
Velocity dispersion	0.05 mesh units/time unit isotropic (58.7 km s^{-1})	0.05 mesh units/time unit isotropic (58.7 km s^{-1}) 0.04849 after correction to same virial state as model A
Rotation velocity	0	π/1000 radians/time unit (18.45 km s^{-1} at 10 kpc radius) 0.003075 after correction to same virial state as model A
$\lvert 2T/W \rvert$ virial ratio	0.975422	(1.01796 initially)
Run time	2526 timesteps (4.21×10^9 yr)	2070 timesteps (3.45×10^9 yr)
Rotational KE/ Random KE	0	0.044296

particle distribution and the Gaussian random isotropic velocity dispersion, were chosen as the simplest possible initial conditions for the first model, without any pretensions to great realism.

The model was followed to 2526 timesteps, which with the time unit quoted above gives a time equivalent to 4.21×10^9 yr. The progress of the collapse, which was rather gentle because the initial conditions were close to virial equilibrium, is shown in terms of the virial parameter $|2T/W|$ in Fig. 1. The failure to return exactly to unity is due to approximations involved in determining W, which has to be interpolated from the values at the closest grid points. This particular algorithm slightly overestimates W, resulting in equilibrium at a virial ratio of rather less than unity. The periodic fluctuations of amplitude ~ 0.01 in $|2T/W|$ which continue to the end of the model suggest that the model has not achieved complete relaxation even at 2526 timesteps. A similar effect has been noted by Garner (1978) in all spheroidal models starting close to virial equilibrium. In a violent collapse, mixing is very thorough, and such oscillations die away quickly, but in gentle collapses mixing appears to continue for a very long time.

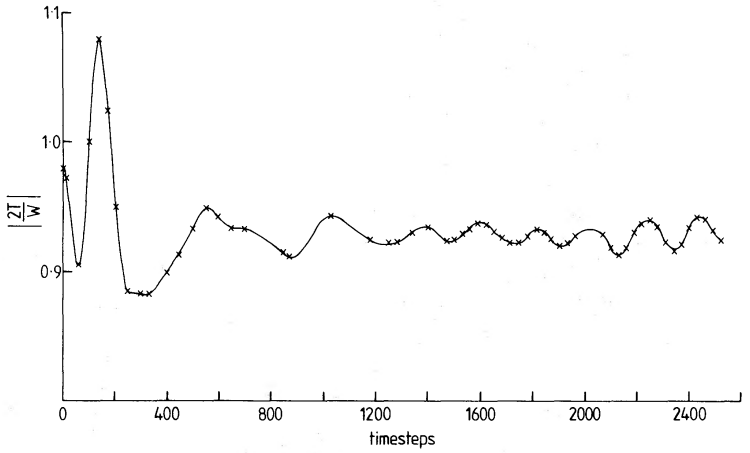

Figure 1. The collapse of model A, as shown by the variation of the virial ratio $|2T/W|$ with time.

Figs 2 and 3 show point plots and contour plots of the final state of the galaxy. The contours are isodensity contours, the density being projected along the line of sight on to the sky plane. The galaxy is always viewed down the inertial frame (mesh frame) x-axis, but after having been rotated through the Euler angles (ϕ, θ, ψ), where ϕ represents the counterclockwise rotation about the z-axis, θ the subsequent counterclockwise rotation about the new x-axis, and ψ the final counterclockwise rotation about the new z-axis. Similar plots are obtained at any time after about 400 timesteps, there being little visible evolution after this stage. The plots are shown in the frame of the mesh, and it is clear that the galaxy has rotated slightly. This is due to the accumulation of angular momentum which is transferred to the galaxy from the mesh because the forces between individual particles are not absolutely isotropic or exactly central. In terms of the units mentioned above, the rotation of about 20° occurring in the last 1000 timesteps amounts to an angular velocity of $1.8\,\mathrm{km\,s^{-1}}$ at a radius of 10 kpc by the end of the run, which is too low to affect the galaxy dynamically, especially since it is acquired after any redistribution due to the collapse has subsided. It is necessary to continue the model for this length of time: (a) to prove that the figure is stable over a period comparable with a galaxy lifetime, and (b) to delineate the orbits properly.

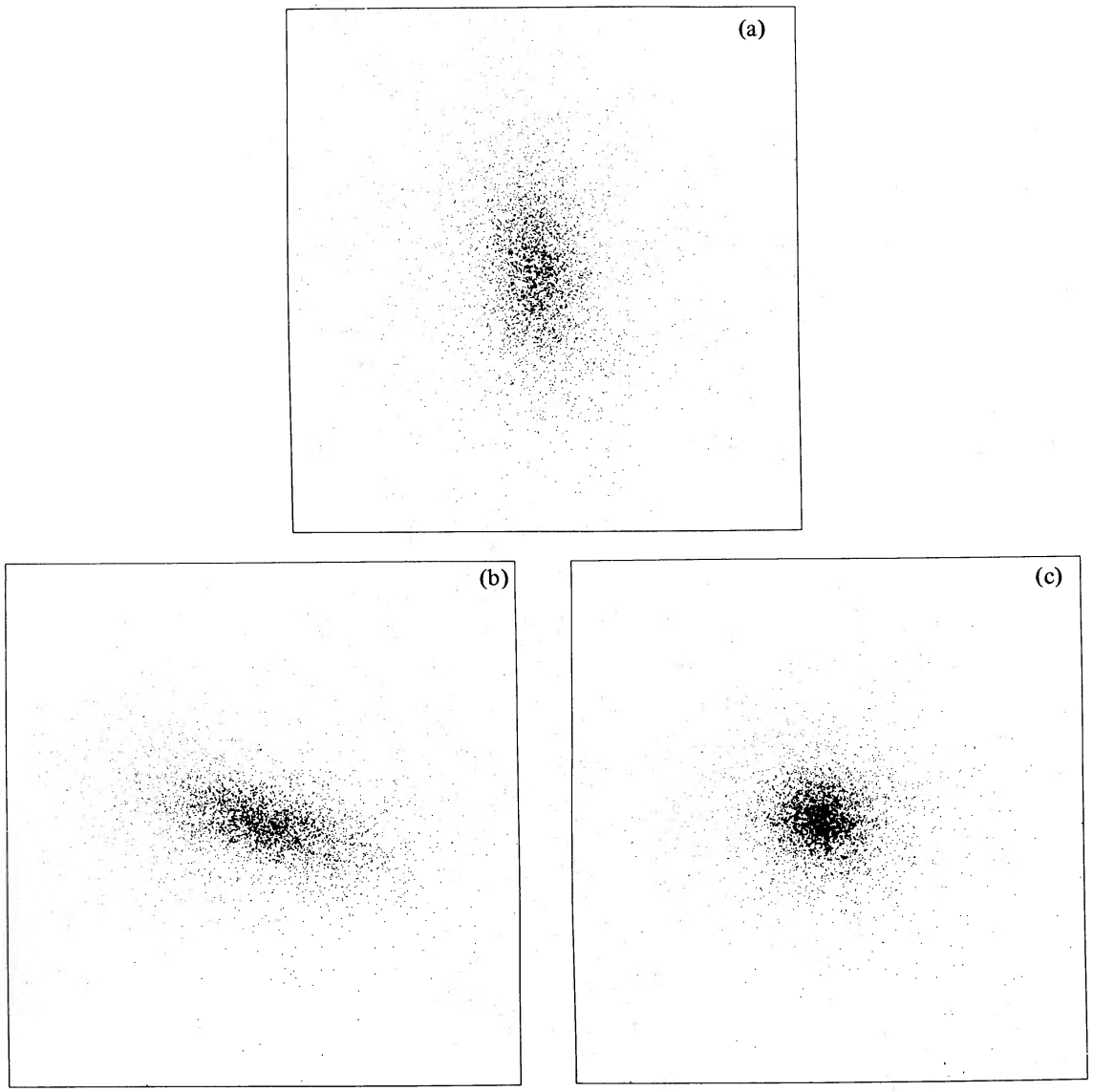

Figure 2. The final state of model A, viewed along the principal axes of the ellipsoid. Only every eighth star is shown. View along (a) z-axis, (b) y-axis, (c) x-axis.

3.2 MODEL B: ROTATING

The geometry and particle distribution were the same as in model A. The velocity dispersion was also initially the same, and each star was given in addition an arbitrary solid body rotational velocity of $\pi/1000$ rad/time unit. The kinetic energy contributed by this rotation was 4.4 per cent of that contained in the random energy of the stars (Table 1), and the rotation therefore represented only a small perturbation of the non-rotating state.* The total velocity for each star was then reduced so that the virial ratio was the same as in model A, in order that the collapse should proceed from the same virial state in both cases. The result was that the actual collapse took place in a model which had slightly less random kinetic energy than model A.

Fig. 4 shows that the collapse as measured by the virial coefficient $|2T/W|$ proceeded in a very similar way to that for model A. The rotating model reached a constantly maintained

* It was not sufficient to balance the components of gravitational force perpendicular to the rotation axis, and the rotation period was not related to the integration interval. [Added in press.]

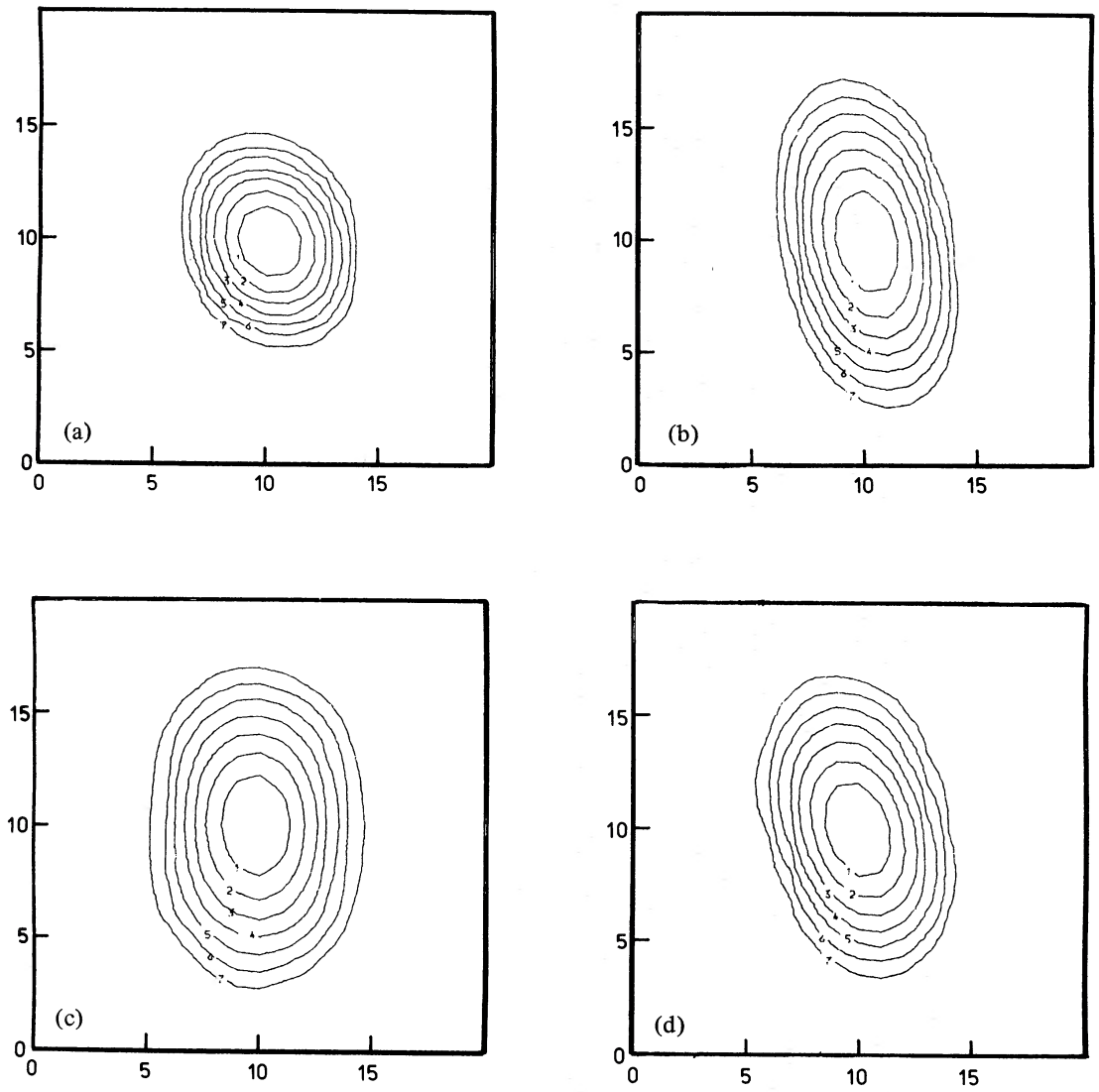

Figure 3. Contours of isodensity integrated along the line of sight and projected on to the sky plane. View along (a) x- or long ellipsoid axis, (b) y- or intermediate axis, (c) z- short, rotation axis, and (d) a general direction given by Euler angles (90, 45, 30). The contours were chosen at logarithmic intervals of one eighth the peak value. Dimensions are given in mesh units.

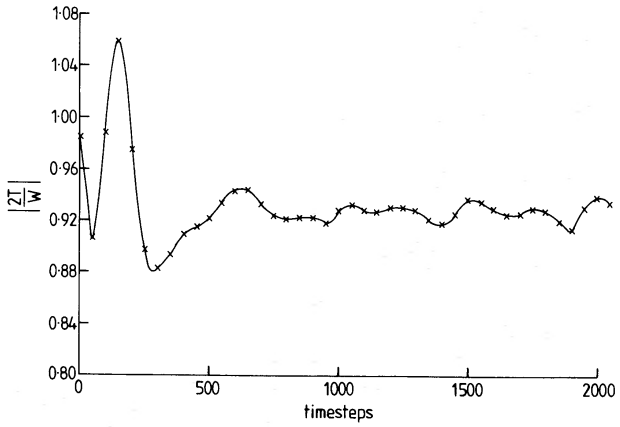

Figure 4. The collapse of model B, shown by the variation of the virial ratio $|2T/W|$ with time.

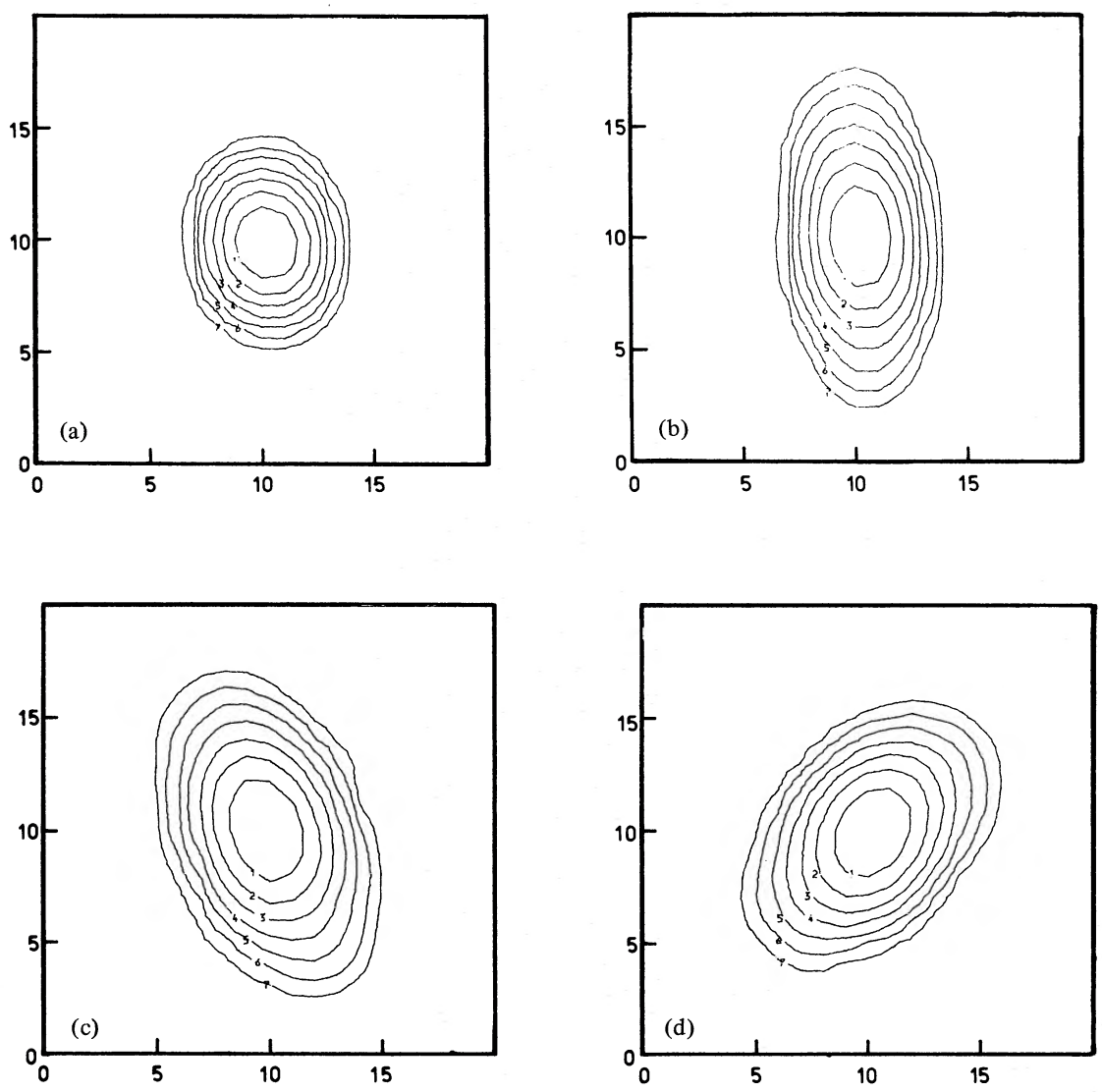

Figure 5. Projected isodensity contours for model B at timestep 1040. Viewpoints as in Fig. 3; the z-axis is the rotation axis. Note the slight twisting between the inner and outer contours seen both along the short ellipsoid axis and the general direction.

value of $|2T/W|$ after about 700 timesteps, and the mean body rotation speed was 0.0022 rad timestep^{-1} (about 0.67 of the initial solid body rotation). However, the detail of the time variation of the density distribution, which is described in Section 4.3 below, is more complicated than in the stationary case. This model was followed for the rather shorter time of 2060 timestep, equivalent to 3.45×10^9 yr. Contour plots of the state of this model at timestep 1040 and at the end of the model are shown in Figs 5 and 6.

4 Properties

4.1 ELLIPTICITY

The projections on to all three principal planes through the models were investigated in order to span the range of ellipticities which might be seen on viewing the galaxy from any angle, and in addition some projections from general angles were examined.

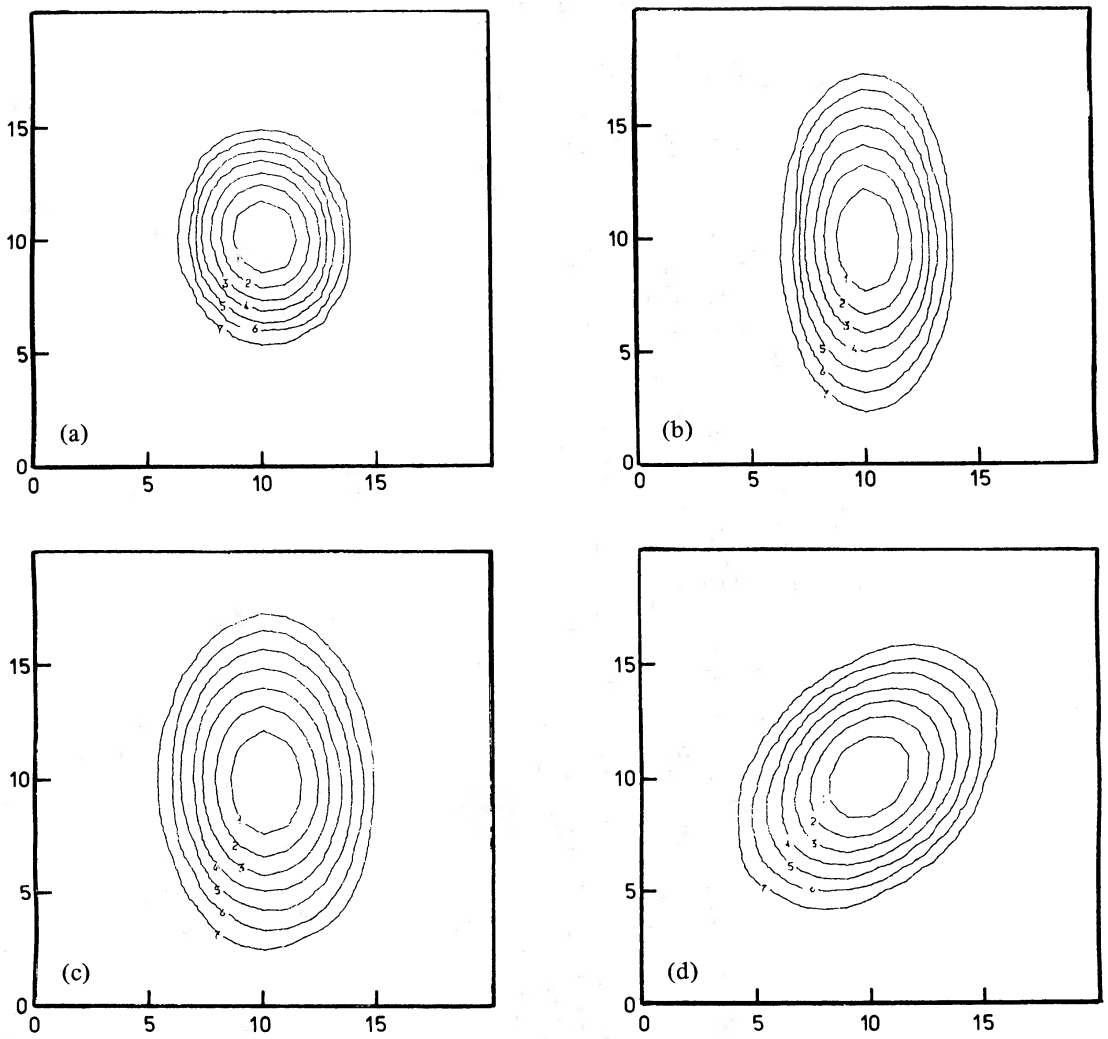

Figure 6. Projected isodensity contours for model B at timestep 2060, viewpoints as in Fig. 3.

Two methods for determining the ellipticity were tried. In the first, ellipses were fitted to the projected isodensity contours, the number counts being linearly interpolated between the adjacent cells to determine the contour positions (a modified version of a program kindly lent by J. Binney was used in this process). Although no detailed study of the deviations of the contours from the ellipses has yet been made, the fits were in general good, and the 'isophotes' were mostly quite close to true ellipses. (The S-shaped contours occurring in the early stages of the evolution of model B, see Section 4.2, are exceptions to this statement.) The fitting process gives the position angle of the major axis, the central offset of the ellipse and the areas within the ellipse and the actual contour. Table 2 contains the details of the ellipses fitted to the final steps of model A and the final step and a step at roughly the half-way point in model B. At this point in model B little physical distortion could be detected, but isophote twisting is still noticeable from a general viewpoint. The reduced χ^2 value for each ellipse fitted is also given in Table 2, and for values less than or equal to unity, the assumed curve can be considered to fit the spread of data points well.

The second method was that described by Young *et al.* (1979), where Fourier coefficients derived by analysing the projected number density round a narrow elliptical annulus yield expressions for the axial ratio, centre offset and position angle of the major axis of a true annular 'isophote'. This method proved less satisfactory for discrete data than for the cor

1982MNRAS.199..171W

Table 2. Ellipticity.

(a) Model A, time 2070

Isophote Stars/mesh unit^2	Semi-major axis mesh units	Ellipticity	Position angle (o)	Centre offset X_o (mesh units)	Centre offset Y_o (mesh units)	Reduced χ^2	Area Inside Contour (mesh units)^2	Area Inside Ellipse (mesh units)^2
a) View down long axis								
184	2.30	0.16	116	0.23	0.05	0.02	14.03	14.04
116	2.88	0.17	116	0.21	0.05	0.06	21.76	21.69
73	3.35	0.17	116	0.21	0.03	0.16	29.36	29.14
46	3.84	0.19	112	0.21	0.07	0.34	37.86	37.71
29	4.30	0.19	113	0.20	0.07	0.37	47.52	47.10
18	4.86	0.20	109	0.15	0.07	0.64	59.34	58.93
b) View down intermediate axis								
199	2.25	0.40	102	0.08	0.11	0.05	9.52	9.33
126	3.40	0.43	102	-0.12	0.10	0.07	20.41	20.56
79	4.32	0.45	102	0.12	-0.13	0.02	32.23	32.35
50	5.13	0.46	101	0.10	-0.10	0.05	44.51	44.62
32	5.96	0.48	101	-0.13	0.15	0.14	57.86	58.03
20	6.72	0.49	101	-0.11	0.16	0.24	73.93	74.06
13	7.49	0.48	100	0.09	-0.15	0.25	91.48	91.61
c) View down short axis								
172	2.17	0.29	93	0.12	-0.16	0.03	10.40	10.44
109	3.22	0.31	93	0.04	-0.18	0.07	22.52	22.45
69	4.10	0.32	92	0.07	-0.15	0.26	36.03	35.85
43	4.92	0.34	92	0.09	-0.17	1.06	50.67	50.34
27	5.70	0.34	91	0.11	-0.16	1.73	67.81	67.42
17	6.40	0.34	91	0.13	-0.13	0.53	86.31	85.08
11	7.100	0.31	91	0.12	-0.14	3.48	110.4	109.2
d) View from Euler Angles (-90, 45, 30)								
206	2.13	0.65	107	0.03	-0.05	0.03	9.08	9.25
130	3.16	0.63	107	-0.06	-0.02	0.01	19.30	19.59
82	3.98	0.62	107	-0.05	-0.02	0.01	30.64	30.75
52	4.75	0.60	105	-0.03	-0.01	0.03	42.34	42.47
33	5.42	0.60	106	-0.05	-0.04	1.57	56.01	55.72
21	6.20	0.59	105	-0.02	+0.08	0.28	71.36	71.53
13	6.82	0.61	104	-0.11	-0.05	4.07	89.28	88.82

Table 2 – *continued*

(b) Model B, time 1040

Isophote Stars/mesh unit^2	Semi-major axis mesh units	Ellipticity	Position angles (o)	Centre offset X_o (mesh units)	Centre offset Y_o (mesh units)	Reduced χ^2	Area Inside Contour (mesh units)^2	Area Inside Ellipse (mesh units)^2
a) View at Euler angles (0 + 90, -50, 0)								
56	2.06	0.24	58	- .03	0.02	.02	10.02	10.11
35	3.62	0.25	56	- .00	0.24	.05	21.45	21.41
22	3.85	0.28	55	- .24	0.02	.03	33.45	33.60
14	4.58	0.30	52	.03	0.23	.29	46.58	46.24
9	5.36	0.31	51	.01	0.23	1.00	61.69	61.15
6	6.09	0.33	48	.02	0.21	2.10	79.65	78.13
4	6.89	0.34	48	.07	0.22	3.57	98.99	98.45
b) Time 2070 View at Euler angles (130 + 90, -50, 0)								
190	1.96	0.20	47	0.03	-0.05	.03	9.63	9.64
120	2.96	0.24	47	0.05	0.01	.01	20.90	21.03
76	3.72	0.25	47	0.05	0.00	.02	32.57	32.75
48	4.39	0.25	46	0.00	-0.05	.19	45.65	45.50
30	5.12	0.27	46	0.01	-0.06	.41	60.32	59.87
19	5.89	0.30	45	0.02	-0.07	.53	77.21	76.83
12	6.61	0.30	46	0.08	-0.07	1.57	97.64	96.57

Table 2 – *continued*

(c) Model B, time 2060

Isophote Stars/mesh unit^2	Semi-major axis mesh units	Ellipticity	Position angles (o)	Centre offset X_o (mesh units)	Y_o	Reduced χ^2	Area Inside Contour (mesh units)^2	Inside Ellipse
a) View down long axis								
297	1.60	.15	104	-0.07	0.17	.02	6.64	6.78
187	2.30	.15	101	-0.09	0.18	.02	13.92	14.08
118	2.85	.16	101	-0.09	0.20	.04	21.52	21.46
75	3.35	.17	100	-0.13	0.18	.10	29.32	29.21
47	3.84	.20	97	-0.12	0.16	.19	37.28	37.07
30	4.25	.19	97	-0.14	0.21	.52	46.27	45.86
19	4.74	.20	94	-0.12	0.16	.40	57.23	56.69
b) View down intermediate axis								
202	2.21	0.38	93	0.17	0.16	.04	9.46	9.53
128	3.23	0.40	91	0.16	0.16	.13	19.95	19.77
81	4.06	0.41	90	0.13	0.17	.47	31.10	30.73
51	4.97	0.44	90	0.11	0.14	.41	43.47	43.12
32	5.72	0.46	90	0.13	0.13	2.22	56.85	55.73
20	6.76	0.50	90	0.19	0.19	.24	72.15	72.30
13	7.45	0.48	89	0.23	0.15	1.72	90.49	90.11
c) View down short axis (rotation axis)								
160	2.21	0.29	93	0.20	0.11	.03	10.84	10.90
107	3.23	0.29	92	0.16	0.19	.08	23.20	23.15
67	4.09	0.31	93	0.14	0.10	.13	36.47	36.24
43	4.91	0.33	92	0.12	0.14	.06	50.92	50.66
27	5.77	0.35	92	0.14	0.13	.07	68.43	68.43
17	6.56	0.35	92	0.17	0.17	1.19	88.03	87.39
11	7.30	0.34	91	0.21	0.17	2.26	111.0	109.8

tinuous data for which it was originally intended, as statistical fluctuations from bin to bin around each annulus were large both in the centre, where the area was small and in the outer regions where there are few stars, and consequently the fits at both ends of the radius range were not reliable. However, it did provide convenient annulus-averaged data for use in determining the radial density distributions.

4.2 TEMPORAL DEVELOPMENT

The variation of the models with time was followed using the first method of determining the ellipticity.

After the initial collapse, the ellipticity as seen along all three principal axes in model A remained fairly constant, and showed a small increase with radius, of about one ellipticity class. No significant change of position angle of the ellipse major axes was observable down any of the principal axes. (By fitting ellipses to the same isophotes viewed down the rotation axis at two different angles, the angular uncertainty was established as $\sim \pm 2^\circ$, and the uncertainty in ellipticity as $\sim \pm 0.02$.) Down a general axis (Euler angles (–90, 45, 30)) a small twist of isophote axis of about 4° was detected.

Model B was more complicated. Its evolution was followed by examining the position angle of the ellipses fitted when viewed down the rotation axis, which varied with both radius and time. Fig. 7(a) shows the angular difference in radians between the inmost and outermost contours as a function of time.

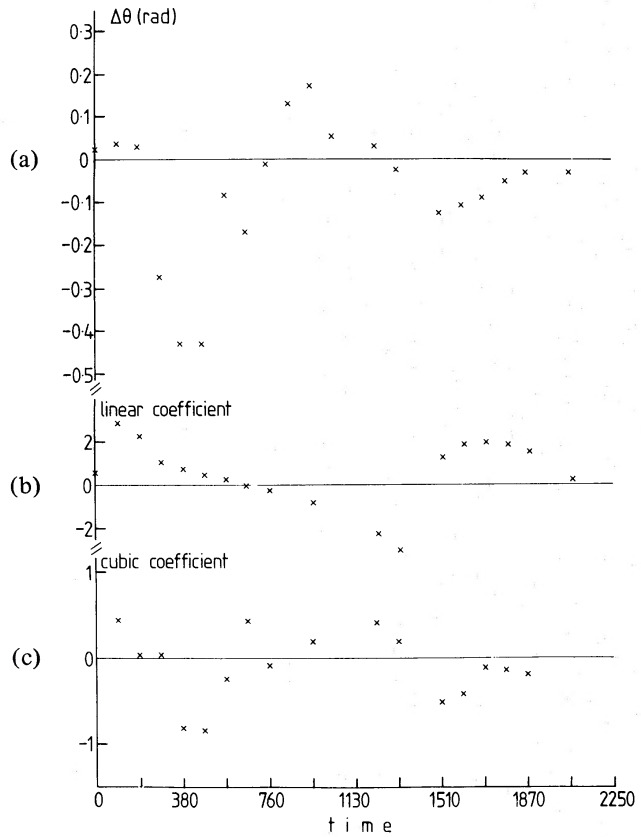

Figure 7. Evolutions of model B. (a) The difference in position angle (in radians) between the major axi of the outer and inner elliptical contours, as a function of time. (b) The variation of the coefficient of th linear term in the expansion of a third-order polynomial fitted to the line passing through the end of th major axis of each elliptical contour. (c) The variation of the coefficient of the cubic term in the sam expansion.

As seen from the fixed mesh frame at first the central part of the model is in advance of the outer, then the outer parts take over the lead, and the oscillation continues with decreasing amplitude as far as the model has been followed. In Fig. 7 (b and c) the result of fitting a cubic polynomial to the line passing through the end of the major axis of each elliptical contour is shown. The top line shows the variation with time of the coefficient of the linear term in the third-order polynomial expansion, and reflects the rotation of the ellipsoid as a whole, while the bottom line is the variation of the coefficient of the cubic term, reflecting the relative deflection of the outer contours. Note the similarity of form between this second curve and that shown in Fig. 7(a).

The amplitude of the oscillation is only a few degrees by the end of the model. The elongated shape of the model causes the behaviour to be displayed rather clearly, the apparent segregation into inner and outer components being obvious because the collapse in the short dimension occurs before that in the long dimension.

The principal axes of the three-dimensional ellipsoidal isophotes are therefore physically not aligned for most of the lifetime of the model. This would cause projections of the isophotes from any random position on to the sky plane to appear twisted. This twisting, which is a real physical distortion, is to be distinguished from the apparent twisting due to projection effects when the ellipticity of the isodensity surfaces varies with radius which is responsible for the 4° twist seen in model A (Binney 1980a; Bennachio & Galletta 1980). Observationally it seems impossible to make this distinction without additional information about the galaxy orientation.

In the model we know that twisting seen when looking directly down the ellipsoid principal axes must be real distortion, and therefore by choosing a time when this distortion is small, we can estimate how much twisting is due to projection effects alone. For example, at time 1320, the rotation axis projection shows a variation of two degrees at maximum, and less than that between the inner and outer isophotes, or in other words, no twisting within the errors. The twist seen from the general viewpoint (−90, 45, 30) at this time is 4°, progressively from the centre to the outside. This is in good agreement with the few degrees predicted theoretically using Stark's analysis, for a case where the ellipticity of the isophotes differs by only approximately one ellipticity class, and with the twisting seen in model A. Unless the ellipticity difference is large, the angular range from which twists of more than a few degrees can be seen due to projection effects alone is small. Therefore in the present model, relative rotation of the isophotes by more than about 6° has to be attributed partly to a real physical twisting of the axes of the isodensity surfaces.

The practical result is that the isophotes do appear to twist by a few degrees when viewed from most general angles, and the ellipticity does increase with radius (Fig. 5d). The effects quite closely resemble the behaviour seen in some real elliptical galaxies (e.g. NGC 323, 6868, 3309, 4816, A2199−45, etc., di Tullio 1979; Bennachio & Galletta 1980) where the projected ellipticity increases by approximately one class as a function of radius and a twist of approximately 20° is seen. As Binney (1980a) and others have suggested that such rotation is due entirely to geometrical projection effects rather than actual physical misalignment, it is pertinent to reconsider whether the conditions which lead to the present misalignment could have any relation to those in which a real protogalaxy might find itself. The necessary factors are rotation accompanied by collapse. Efstathiou & Jones (1979) have shown that rotation sufficient to give a typical elliptical galaxy a value of the ratio

$$(V_{\mathrm{rot}}/\sigma_{\mathrm{peak}})_{\mathrm{median}} = 0.22$$

could have been acquired during primordial interactions with neighbouring masses. Such a ratio could be achieved with values of $V_{\mathrm{rot}} = 33\,\mathrm{km\,s^{-1}}$, $\sigma_{\mathrm{peak}} = 150\,\mathrm{km\,s^{-1}}$ which would be equivalent to a rotation velocity of 0.006 rad timestep^{-1} at 10 kpc in a model. As this is

roughly twice the actual rotation velocity used, there is no difficulty in postulating that this amount of rotation could have been added before or during the collapse phase.

Binney & Silk (1979) have pointed out that the elongated shape would be the principal result of primordial encounters, and although this shape is not necessary for the concept of the two-part collapse, it results in the effects being more clearly seen.

It should also be re-emphasized that only ~8 per cent of the sample considered by Bennachio & Galletta (1980) showed rotations of more that 15°. We would therefore need to invoke rotation during an anisotropic collapse for only a rather small percentage of galaxies on this model. Although the details of the present model are not realistic, it is clear that the type of initial conditions represented here are not totally implausible, and work is at present in progress on a model incorporating rather more realistic conditions.

4.3 DENSITY PROFILE

The radial density profile changed rapidly during the initial collapse phase, taking on the form which was maintained throughout the rest of its evolution by about timestep 500 in both models. The two methods used in the determination of the ellipticities also provided the density profile data, in terms of the number of stars per square mesh unit either on a particular contour or averaged over a particular annulus at constant $s = \sqrt{ab}$. The length scale is expressed dimensionlessly as $s/s_{1/2}$, where $s_{1/2}$ is the s value of the ellipse which contains half the mass in the given projection. The density value given in the first filled ellipse in Young's method is taken as a measure of the central density I_0, and the densities are plotted as $\log I/I_0$.

The density follows approximately a Hubble law (s^{-2}) when viewed down the rotation axis, but is rather steeper when viewed from the other two principal directions, having a

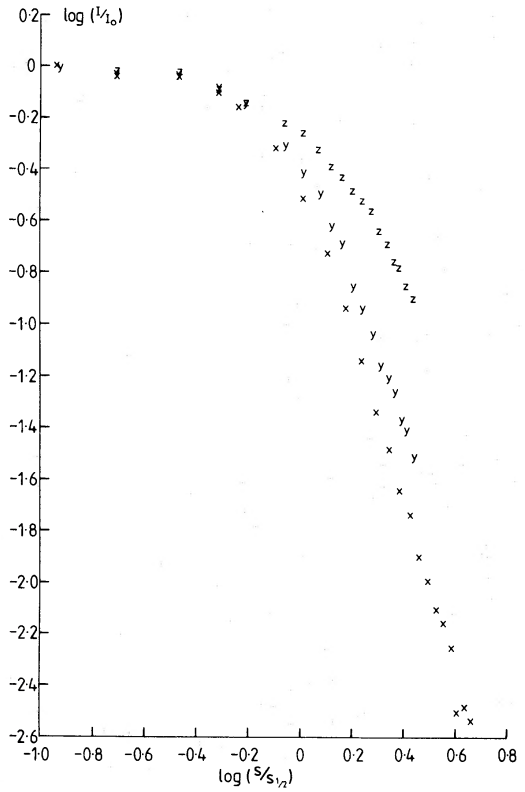

Figure 8. Projected density profile down each of the three principal axes, averaged over ellipsoidal annuli.

slope of ~ -3 (Fig. 8). The power law continues as far as the curve can be followed, which is the point where there are so few stars that the mean densities become unreliable.

Very few real galaxies have a density fall-off steeper than the Hubble law, and in many cases it is less steep (see, e.g. Kormendy 1977), which is one aspect in which the present models are unrealistic. This may perhaps be a reflection of how well mixed the model is by the time the important part of the relaxation is completed; van Albada (1980) has shown that more violent collapses become better mixed.

Real galaxies, especially those which do follow the Hubble law well, also continue to follow a linear relation closer in to the centre of the galaxy than our models (Kormendy 1977). Some galaxies have steeper central profiles, fitting the more strongly peaked de Vaucouleurs law ($\log I \propto s^{1/4}$) until very close to the centre, and some are even more centrally enhanced than this (e.g. NGC 6251, M87, Young *et al.* 1979, King 1978), though Schweizer (1979) has noted that this may be a seeing effect. The interpretation of these very peaked profiles is still controversial, but it is clear that we cannot expect to be able to reproduce them with the present code, for the reasons connected with resolution given in Section 2. This inability to produce a realistic density distribution is probably the most serious defect of the present model. It has proved a difficulty for previous models too; for example, Aarseth & Binney (1978) found a rather steeper slope than a Hubble law for their triaxial model. Mergers, however, appear to be more successful at producing the observed power law than single galaxy collapses; the mergers produced by Simon White (1978) were close to power laws with index -2. The compound orbital model approach, as used by Schwarzschild (1979), has the advantage in this respect in that the density law is chosen initially to be realistic.

4.4 VELOCITY CONTOURS

The slow rotation indicated by the major axis velocity profiles obtained by Bertola & Capaccioli (1975) and Illingworth (1977) was the first indication that elliptical galaxies may not be rotationally flattened. The apparent rotation curve is therefore an important aspect of any model. Fig. 9 shows the contours of projected line of sight velocity for the rotating model (B) along the intermediate principal axis and a general viewpoint, after 2060 timesteps. Model A as expected shows no systematic velocity structure.

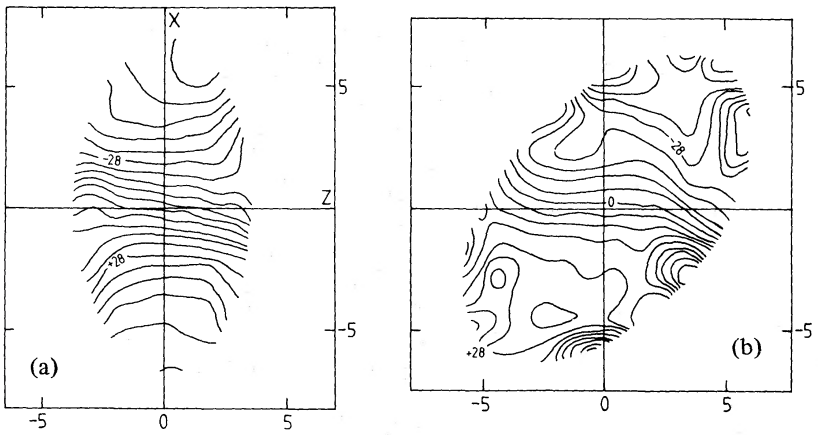

Figure 9. Contours of projected line of sight velocity in km s^{-1} for the rotating model B. Length scales are in mesh units. (a) Line of sight is ellipsoid intermediate axis. (b) Line of sight is the general viewpoint given by the Euler angles (90, 45, 30). Dimensions are given in mesh units.

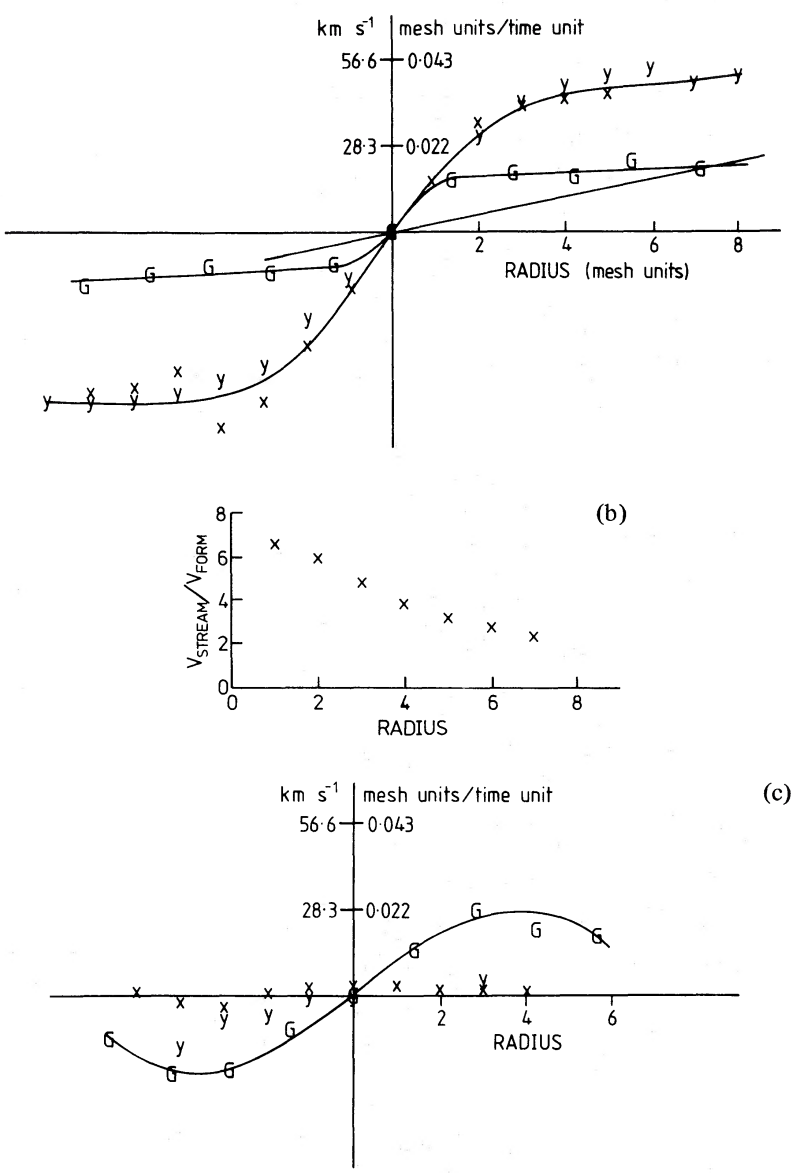

Figure 10. Projected line of sight velocities for model B. (a) Major axis rotation curves, seen down the long (x) and intermediate (y) axes and from a general viewpoint (G). The straight line is the rotation curve of the form of the ellipsoidal body. (b) The ratio of bulk streaming velocity to form velocity as a function of radius. (c) Minor axis rotation curves, seen down the long (x) and intermediate (y) axes and from a general viewpoint (G). Significant minor axis rotation is seen from the general viewpoint.

The major axis rotation curves of the views down the x- and y-axes and from the general viewpoint are shown in Fig. 10(a), and the minor axis equivalents in Fig. 10(c). The units along the velocity axes have been given both in mesh units per timestep and in km s^{-1} as appropriate to the galaxy model discussed above. The maximum velocities here correspond exactly to the observational V_{peak} used by Binney (1980b) to characterize galaxy rotation. The flat major axis curves bear a strong resemblance to those of real galaxies (Illingworth 1977; Davies 1978; Peterson 1978 etc.). The significant rotation about the minor axis seen from a general viewpoint illustrates the prediction of Contopoulos (1956), that if the body is triaxial, then minor axis rotation should be observable. However the velocity contours (particularly Fig. 9b) show that single cuts down either apparent axis can give a misleading picture of the rotation, and illustrate the need for complete velocity maps.

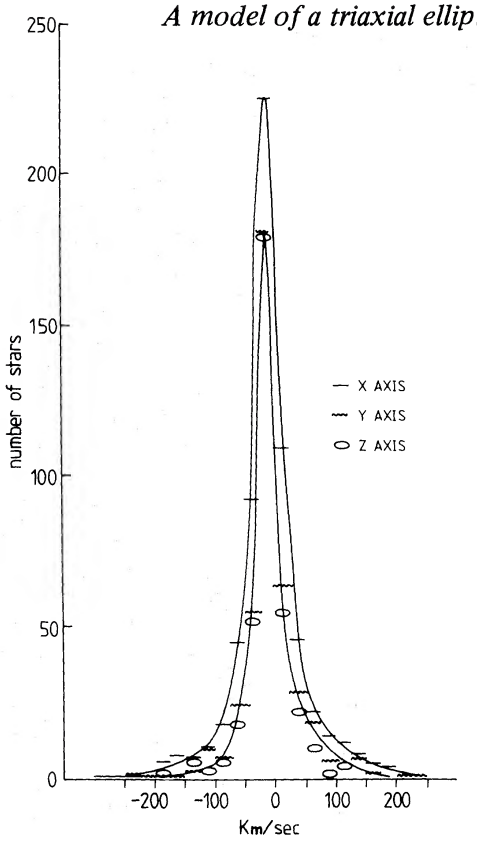

Figure 11. Model B velocity distribution along the line of sight through the centre of the model, viewed along each principal axis. The lines are eye estimates of best fit curves through the x- and y-axis points.

Since the solid body motion of the ellipsoid is known from the projections along the rotation axis it is possible to separate the component of velocity which is due to the body rotation and that due to bulk streaming of particles around the body. The straight line in Fig. 10(a) shows the rotation curve of a solid body rotating at the mean speed of the ellipsoid. The ratio of streaming to body rotation, $v_{\text{stream}}/v_{\text{form}}$, varies from about 6 at small radii to about 2 at radii of about seven mesh units, as shown in Fig. 10(b). A large-scale measurement like this does not give any information about the sense of motion of individual orbits, but does imply that the majority are prograde at any given time.

The distribution of the velocities along the line of sight is shown in Fig. 11. The broadening of the wings of the distribution with respect to a pure Gaussian distribution is due to the finite area of the cell which is considered to contain the central stars in the galaxy, some of which will have a rotational component.

4.5 PROJECTED VELOCITY DISPERSIONS

The variation of velocity dispersion with radius is presented as major axis profiles for model B in Fig. 12, for views along all three principal axes. Contours are shown in Fig. 13 from two view points for model B; unfortunately we do not have the resolution to be able to trace details of the behaviour into the crucial central region. Binney (1980c) has suggested that a peak density distribution will result in a dip in the centre of the velocity dispersion profile, but we can say little more than that our profiles decrease steadily with radius, in common with ~ 50 per cent of observed ellipticals (Illingworth 1977).

Table 3 illustrates that the ellipsoidal shape is indeed maintained by anisotropic pressures, the values given being those at the peak of the distribution in the centre of the galaxy. These peak values have also been used together with the appropriate rotation curve to estimate the

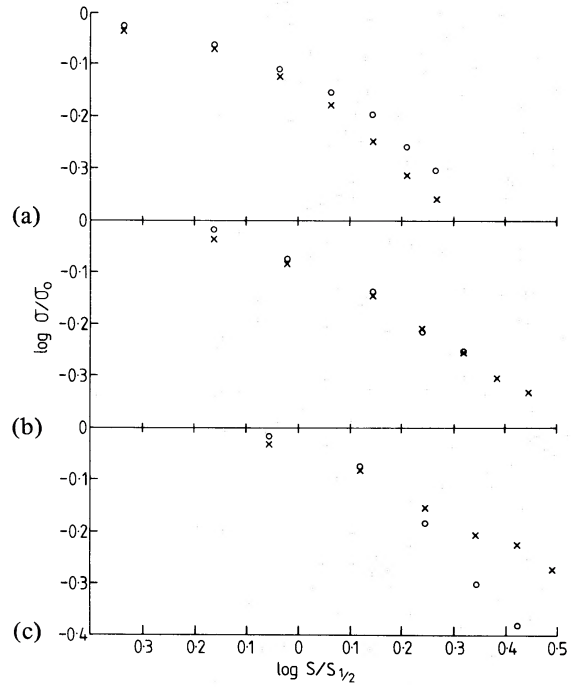

Figure 12. Model B velocity dispersion profiles, (x) major axis and (○) minor axis for each of the projec tions. (a) Down rotation axis. (b) Down intermediate axis. (c) Down long axis.

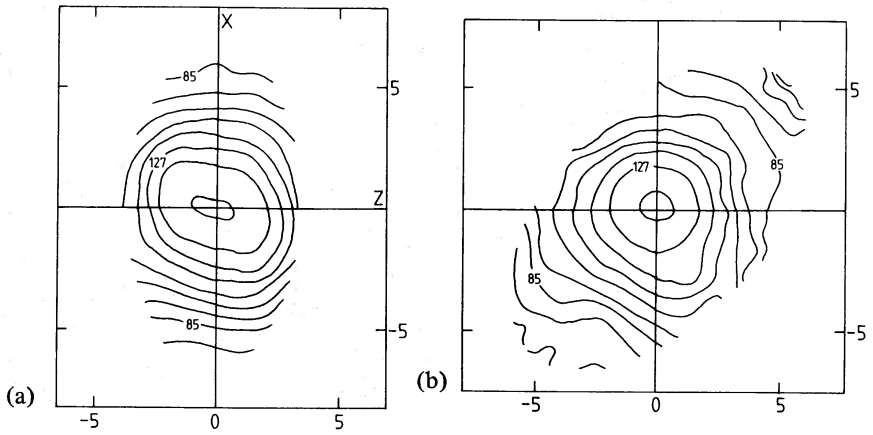

Figure 13. Contours of projected velocity dispersion for model B at time 2060, viewed down (a) the inter mediate axis and (b) from the general viewpoint (90, 45, 30). Dimensions are given in mesh units.

Table 3. Projected line of sight velocity dispersions as a measure of anisotropic pressures.

Model B

Time step	Major axis σ_{11}	Intermediate axis σ_{22}	Minor axis σ_{33}
1040	170.0	142.8	119.6
2060	166.9	144.3	119.1

Units: km s^{-1} when model scaled for typical elliptical galaxy as described in Section 3.1.

values of V_{max}/σ_{peak} to enable comparison of the models with both observational result and previous models in terms of the well-known diagram of V_{max}/σ_{peak} against ellipticity (Fig. 14). The range of ellipticities covered by the present models (cross-hatched) is tha indicated by the maximum to minimum real ellipticities given by the fitted contours seer from different directions.

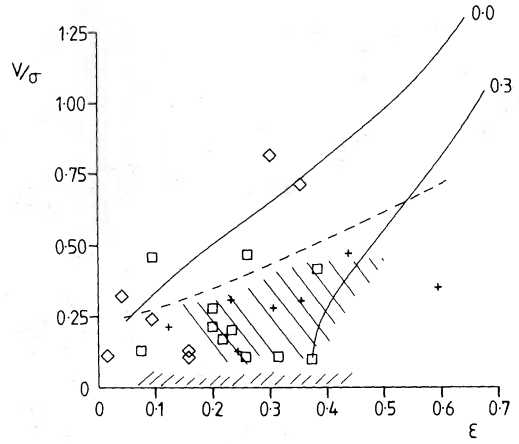

Figure 14. The relation between V_{max}/σ_{peak} and ellipticity. Some observed values are shown as crosses (Illingworth 1977), squares (Schecter & Gunn 1979) and diamonds (Davies 1981). The full curves are Binney's (1980b) relations for oblate spheroidal models with pressure anisotropy parameter $\delta = 0$ and 0.3. The dashed line is the line about which prolate spheroidal galaxies with $\delta = 0$ would lie if randomly oriented. The cross-hatched areas indicate the ranges occupied by the present models at various projections.

4.6 VELOCITY ELLIPSOIDS

The variation of the velocity ellipsoid with position in the principal plane of the model can be determined by considering the velocities of stars lying near principal sections through the galaxy at the end of the model evolution. Stars lying within one mesh space of the principal plane in question were selected. The by now substantial symmetry of the model was exploited by using stars in all four quadrants folded on to the top right quadrant so that the results could be presented in a single quadrant only. For each of the 15×15 mesh cells in this quadrant the number of stars in the cell, the mean velocities $\langle v_i \rangle$ and the six components of the tensor $\langle v_i v_j \rangle$ were stored. The velocity dispersion tensor $\sigma_{ij}^2 = \langle v_i v_j \rangle - \langle v_i \rangle \langle v_j \rangle$ was then calculated in each cell. Following the method used by Merritt (1980), by diagonalizing the σ_{ij}^2 matrix, the components were transformed into the three principal dispersions giving the axial dimensions of the velocity ellipsoid, and the three direction cosines relating these axes to those of the figure. In Fig. 15 the projections of the two longest principal axes of each velocity ellipsoid on to the principal planes are shown for both models. It is noticeable that in both models the ellipsoids align parallel to the model form axes in the centre of the galaxy, as Binney (1980b) has pointed out must happen in an anisotropy-pressure dominated galaxy where the velocity dispersion anisotropy must be constant at the centre. In the outer parts of the galaxy the alignment is approximately radial as expected, though the decreasing number of stars in each bin with each radial increment causes the pattern to become unclear beyond about six or eight mesh units. The effects of the rotation upon the final state of model B appear to be negligible.

These diagrams are directly comparable with those describing Schwarzschild's model as given by Merritt (1980). The most noticeable difference is that our models show the alignment with the galaxy form axes over a larger region than in the Schwarzschild model and the outer radial trend is less marked. This may be partly due to the above mentioned statistical difficulties with outer parts of our model, and may also be a result of the differing density profiles.

An estimate of the variation of the radial dispersion σ_r^2 with radius has been obtained by plotting the principal dispersion which is aligned most closely to the radial direction as a function of radial distance. The curves labelled 'R' in Fig. 16 show such results for model A.

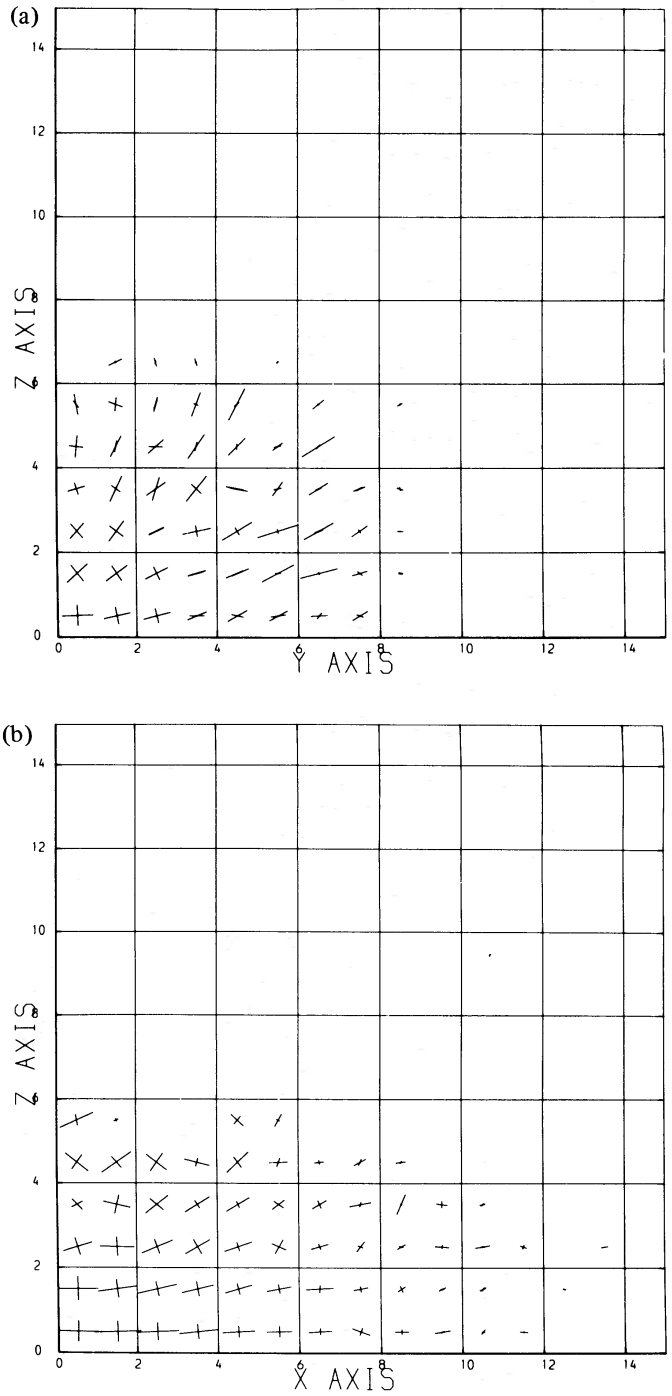

Figure 15. Projections of the velocity ellipsoids in the galaxy principal sections on to the correspondir principal planes for model A at time 2526. (a) *yz*-plane, (b) *xz*-plane, (c) *xy*-plane.

As in Merritt's work, the mean curve is like that of a truncated isothermal sphere, showing gradual decline with distance from the centre.

Similarly, by considering the principal dispersion most closely perpendicular to the radiu vector estimates of σ_ϕ^2 have been obtained and are shown in Fig. 14 as the curves labelle 'T'. The radially directed principal dispersion, taken along the rotation axis only, yielde estimates of σ_z^2. All dispersions decreased with radius, though σ_z^2 did so less markedl than σ_ϕ^2 and σ_r^2. The major axis value of σ_r^2 was greater than the minor axis value, as woul

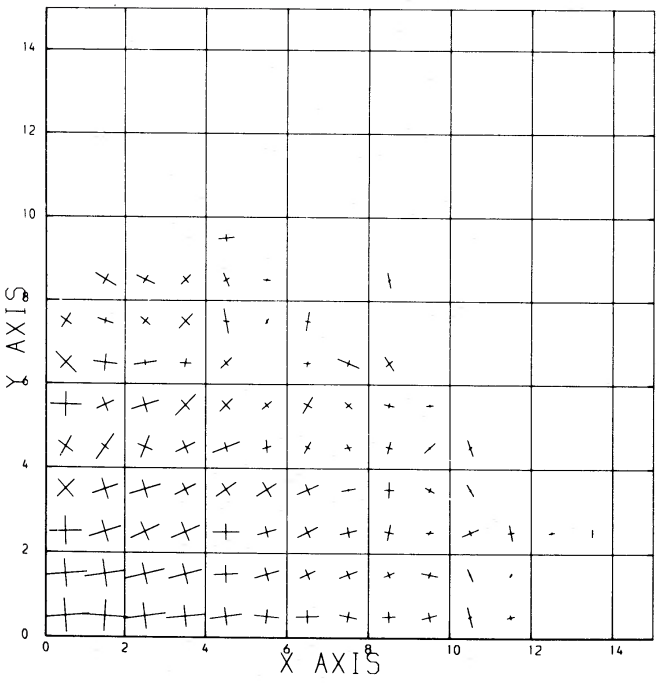

Figure 15(c)

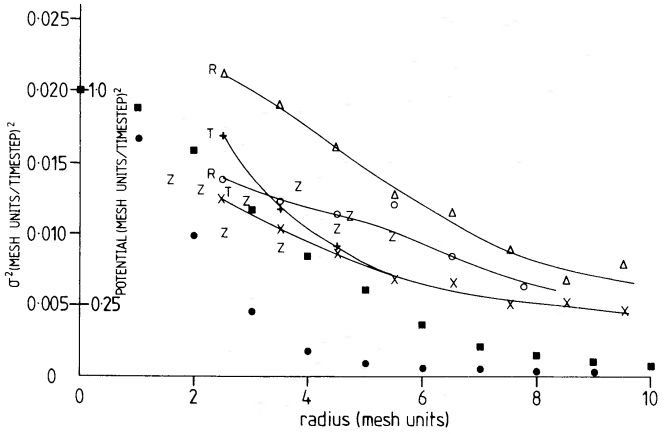

Figure 16. Projections of radial, tangential and axial velocity dispersions with radius. The upper radial (R) curve (△) is for the radial component in the major axis direction, while the lower (○) is in the intermediate axis direction. Similarly, the upper tangential (T) curve (+) is taken along the major axis and the lower (×) along the intermediate axis. The axial variation is indicated by the letter (Z). The gravitational potential along the major and intermediate axes is shown by the filled squares and circles respectively, on a scale normalized to unity at the centre of the galaxy.

be expected in order to maintain the anisotropic geometry of the model, with a corresponding increase in the minor axis value of σ_ϕ^2 over the major axis value. σ_z^2 was less than σ_r^2 over the whole range, but of the same order as σ_ϕ^2. All these observations are only qualitative because of the high level of uncertainty particularly at large radii, and can give no information about the centre of the galaxy because of the spatial resolution difficulties.

5 Individual stellar orbits

5.1 STATIONARY MODEL

As has been beautifully illustrated by Schwarzschild (1979), it is possible to construct a self-consistent model of a triaxial ellipsoidal system from orbits belonging to two very simple

families of orbits. It is therefore of great interest to determine whether these families would be the ones which would arise naturally in evolving models such as those presented here.

For 429 stars randomly distributed in starting position throughout the model, the position and velocity were stored at each timestep. The orbits were then reconstructed in the three-dimensional image space of the Manchester University Graphics Unit Vector General display. The direction from which the two-dimensional projections of the orbit were viewed were selected manually, and in this way a good idea of the real three-dimensional orbit shape and orientation with respect to the ellipsoidal body were obtained. In addition the mean angular momentum round each of the principal body axes was recorded as well as the maximum and minimum radii and velocities and the times at which they occurred, and the number of timesteps between turning points in each of the three principal directions. The type of each orbit was noted, and whether it supported or opposed the general sense of the ellipsoidal body.

The fact which is most immediately obvious is that there are very few types of orbit involved, essentially just box orbits and orbits in the rosette-tube family. Box orbits are the three-dimensional orbits whose projection show concave sides and rectangular corners where the whole of the volume accessible to the box has been well explored (Ollongren, 1962). The properties of both types of orbit are discussed further in Schwarzschild (1979) and Heiligman & Schwarzschild (1979). Table 4 shows how the stars are distributed amongst the various orbit types in model A, and contains equivalent information for Schwarzschild's triaxial model (D. Merritt, private communication). The two models, which are very similar in final shape, are pleasingly also similar in orbital content. The extra angular momentum carrying orbits (the rosette-tube type) in Schwarzschild's model, which contribute mainly in the central few core radii (D. Merritt, private communication) may reflect the difference in density profiles in the two models.

The fact that very few orbits fall outside the broad box and tube classifications gives a nice confirmation of the generality of the orbit types chosen by Schwarzschild to give a self consistent solution in his chosen potential. Our models have no predetermined condition imposed upon the orbital types, and yet the same orbital families, in similar ratios, arise naturally in the triaxial final shapes into which the galaxies evolve.

Table 4. Stellar orbits.

Percentage of stars occupying each orbit type

	Schwarzschild model*	Model A	Model B
Box true	67.9	74.1	43.1
Pillbox			35.6
True and pillbox			78.7
Rosette			
round x-axis		6.0	3.7
round z-axis		7.4	6.0
Tube			
round x-axis	32.1	3.2	0.95
round z-axis		0.5	2.35
Rosette and tube		17.1	13.0
Other		4.2	3.7
Offmesh		4.6	4.6

*The figures in this column are the percentage of mass contributed by various orbit types in Schwarzschild's non-rotating model.

Table 5. Stellar orbits.

Percentage

Stable, bar supporting	Probably stable, mostly bar supp.	Stable, not bar supp.	Rosettes, not included in previous classes*	Probably really unstable	Other	Off mesh
Model B						
38.9	22.7	21.8	6.5	5.1	0.5	4.6
61.6		28.3				
Model A						
64.8		26.4		4.2		4.6

*Some rosettes lie in bar supporting classes.

The stability of the final shape of the model is suggested by examining the pictures made every 10 timesteps. Very little change in shape is apparent after about the first 500 timesteps, and by about 800 timesteps the fluctuations in the virial parameter $|2T/W|$ have died down almost completely. The orbits confirm that the triaxial state is a stable one. As shown in Table 5, 64.8 per cent of all the orbits and 82.5 per cent of the box type orbits support the sense of the ellipsoid, so 65 per cent of the mass is moving in such a sense as to reinforce the ellipsoidal bar. Of the rosette-tube orbits, equal numbers stream in each direction, consequently adding no net angular momentum to the final model. The type of the orbit does not appear to change once established, and very few orbits show any sign of re-alignment over the whole lifetime of the model.

The ratios of the periods of oscillation in each of the principal directions were found to lie close to 1.15 and 1.55 (Fig. 17) with not very much scatter. This suggests that the ellipsoid arises from a modified 2:2:3 resonance.

Even without detailed investigation, it is obvious that most of the orbits do not fill the ellipsoidal potential volumes available to them, i.e. are not ergodic, which implies the presence of non-classical integrals of motion. We make no attempt in this paper to determine the nature of these integrals, but this is clearly an interesting point to which attention must be given.

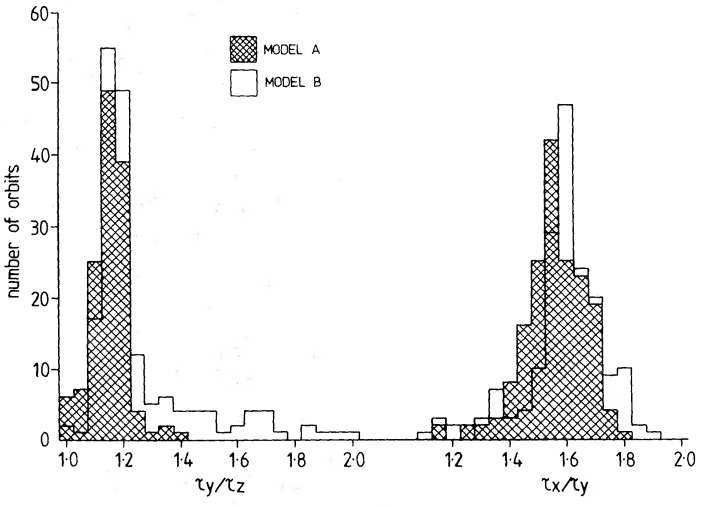

Figure 17. Histograms of the ratios of the orbital oscillation periods.

5.2 ROTATING MODEL ORBITS

Table 4 gives the proportion of each type of orbit for this model. The most interesting development is that a new distinct type of orbit has appeared, which looks like a box orbit when viewed along any direction perpendicular to the rotation axis, but which has a circular rosette-like appearance when viewed along the rotation axis in a frame rotating at the same rate as the ellipsoidal body. These orbits are therefore usually quite distinct from box orbits rotating with the ellipsoid, which would have the usual rather rectangular shape in such a frame. This morphology has led us to the name *pillbox* to distinguish these orbits. It is not always easy to separate a rather square true box orbit from a pillbox orbit because the whole volume available to the orbit cannot be well filled in a galaxy lifetime, and it is therefore possible that a small percentage of the box orbits may have been wrongly classified in this study. Further work involving longer orbits should elucidate the matter. It should however always be possible to separate the pillboxes from z-rosettes because of the significant angular momentum carried by the z-rosettes.

It is possible to find a rotating frame for each pillbox orbit in which it is stationary by assuming that the orbit passes through only two pericentres in one rotation, and determining the angle traversed in the time between alternate pericentres. The speed of such a frame was determined for all the box-like orbits, and a histogram of the speeds obtained appears in Fig. 18. The separation into orbits trapped at the pattern speed of the overall ellipsoidal body at 0.002 rad timestep^{-1} and those not trapped, but having a wide spread of velocities (mostly slower than the pattern and some even counter-rotating to it), is very clear. It should be emphasized that we are talking about the sense of rotation of the frame in which the orbit is stationary and *not* the sense of streaming in the individual orbit. The actual direction of motion of the star changes each time the limiting potential surface is encountered in both box and pillbox orbits. The population of non-trapped orbits is almost entirely made up of the pillbox orbits, while the peak formed by the trapped orbits is composed of genuine box orbits.

The sense in which these orbits begin to move with respect to the stationary frame was noted. Approximately equal numbers of the non-trapped stars set out in each sense, whereas

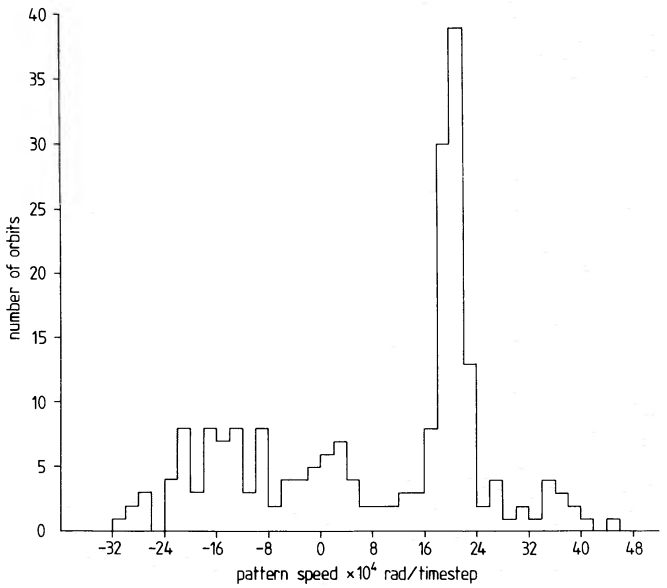

Figure 18. Histogram of the speeds of the pattern-stopping frames for all box type orbits in rotating model B.

roughly twice as many of the trapped stars set out in the same sense as that of the ellipsoid rotation. It seems therefore that there must be some factor other than the position which the star occupies in the initial velocity distribution which decides whether it is trapped or not.

The maximum radii of all the orbits with small and negative pattern speeds were also noted and most were found to be small, 73.5 per cent having mean radii of four mesh units or less, compared with only 41 per cent for the trapped box orbits. This suggests that the initial position of the star, or the part of the potential which influences it most strongly during the initial collapse phase, may also play a part in determining the type of orbit and the state of trapping. There were a few orbits which might have been in the process of changing type, but these were a small minority.

The division into two main types of behaviour brings us back to the division into an inner and outer region remarked upon in Section 4.2 when describing the oscillatory evolution of the rotating model, since the bulk behaviour of the model must necessarily be a composite of that of the individual stars. Tentatively we suggest that the outer parts of the ellipsoid are formed mainly by trapped stars, which starting in the elongated outer parts of the body always see a strong bar-shaped potential. The more spherical inner parts, which are not very closely coupled with the outer parts, would then be composed of the untrapped pillbox orbits, the increased sphericity being explained by the fact that orbits can be found at many orientations to the ellipsoidal outer parts at any given instant. The fact that perpendicular to the rotation axis the pillbox orbits are more or less indistinguishable from the box orbits means that the overall shape of the ellipsoid is not distorted significantly.

Speculation on the mechanism causing the oscillatory behaviour appears to be premature at this stage. Further work on this and on the nature and of isolating integrals and the origin of the pillbox orbits, is at present under way.

6 Conclusions

(1) Evolving triaxial ellipsoidal models can exist for at least 4×10^9 yr.

(2) Slowly rotating triaxial ellipsoids have many properties which are promisingly like those of observed elliptical galaxies.

(3) The important factor in the rotating model is that the rotation and the initial collapse from an asymmetric shape occur simultaneously. Although these conditions have only been introduced in a very simple way at present, the results suggest that it will be important to explore this type of initial situation more closely.

(4) The slow reduction in the oscillation in the rotating model may imply that triaxial symmetry is the most complicated symmetry which an elliptical galaxy can maintain over long periods of time. We are indebted to Professor Schwarzschild for this insight.

Acknowledgments

We thank Bernard Jones for introducing us to this problem, James Binney for encouraging us to pursue it and for the loan of analytical codes, and Professor Schwarzschild for invaluable discussions and inspiration.

We should like to acknowledge our indebtedness to Dr R. H. Miller and A. May for drawing our attention to an error in the time scaling of the original version of this paper. A. May also gave assistance with the analysis of the results. We have profited from discussions with Mr G. S. Mani on projection effects, and would also like to thank the staff of the Graphics Unit of the University of Manchester Regional Computer Centre for help on many occasions.

References

Aarseth, S. J. & Binney, J. J., 1978. *Mon. Not. R. astr. Soc.*, **185**, 227.
van Albada, T. S., 1980. *Contribution to Galaxy Workshop*, Leiden.
van Albada, T. S. & van Gorkom, J. H., 1977. *Astr. Astrophys.*, **54**, 121.
Barbon, R., Benacchio, L. & Capaccioli, M., 1976. *Astr. Astrophys.*, **51**, 25.
Bennachio, L. & Galletta, G., 1980. *Mon. Not. R. astr. Soc.*, **193**, 885.
Bertola, F., 1980. *Proc. NATO A.S.I. Normal Galaxies*, eds Fall, S. M. & Lynden-Bell, D., Cambridge University Press.
Bertola, F. & Capaccioli, M., 1975. *Astrophys. J.*, **200**, 439.
Bertola, F. & Galletta, G., 1979. *Astr. Astrophys.*, 77, 363.
Binggelli, B., 1980. *Astr. Astrophys.*, **82**, 289.
Binney, J. J., 1975. *DPhil thesis*, University of Oxford.
Binney, J. J., 1976. *Mon. Not. R. astr. Soc.*, **177**, 19.
Binney, J. J., 1979. *Comm. Astrophys.*, **8**, 27.
Binney, J. J., 1980a. *Phil. Trans. R. Soc. A*, **296**, 329.
Binney, J. J., 1980b. *Proc. NATO A.S.I. on Normal Galaxies*, eds Fall, S. M. & Lynden-Bell, D., Cambridge University Press.
Binney, J. J., 1980c. *Mon. Not. R. astr. Soc.*, **190**, 873.
Binney, J. J. & Silk, J., 1979. *Mon. Not. R. astr. Soc.*, **188**, 273.
Capaccioli, M., 1979. *Proc. Conf. on Galactic Photometry*, Austin, Texas, 1979 August.
Carter, D., 1978. *Mon. Not. R. astr. Soc.*, **182**, 797.
Contopoulos, G., 1956. *Z. Astrophys.*, **39**, 126.
Davies, R. L., 1979. *PhD thesis*, University of Cambridge.
Davies, R. L., 1981. *Mon. Not. R. astr. Soc.*, **194**, 879.
Efstathiou, G., Ellis, R. S. & Carter, D., 1980. *Mon. Not. R. astr. Soc.*, **193**, 931.
Efstathiou, G. & Jones, B. J. T., 1979. *Mon. Not. R. astr. Soc.*, **186**, 133.
Evans, D. S., 1951. *Mon. Not. R. astr. Soc.*, **111**, 526.
Galletta, G., 1980. *Astr. Astrophys.*, **81**, 179.
Garner, G. L., 1978. *PhD thesis*, University of Manchester.
Heiligman, G. & Schwarzschild, M., 1979. *Astrophys. J.*, **233**, 872.
Hohl, F., 1978. *Astr. J.*, **83**, 768.
Illingworth, G., 1977. *Astrophys. J.*, **218**, L43.
James, R. A., 1977. *J. Comp. Phys.*, **25**, 71.
James, R. A. & Sellwood, J. A., 1978. *Mon. Not. R. astr. Soc.*, **182**, 331.
King, I. R., 1978. *Astrophys. J.*, **222**, 1.
Kormendy, J., 1977. *Astrophys. J.*, **218**, 333.
Liller, M. H., 1960. *Astrophys. J.*, **132**, 306.
Liller, M. H., 1966. *Astrophys. J.*, **146**, 28.
Lin, C. C., Mestell, L. & Shu, F. H., 1965. *Astrophys. J.*, **142**, 1431.
Merritt, D., 1980. *Astrophys. J. Suppl.*, **43**, 435.
Miller, R. H., 1978. *Astrophys. J.*, **223**, 122.
Miller, R. H. & Smith, B. F., 1979. *Astrophys. J.*, **227**, 407.
Miller, R. H. & Smith, B. F., 1981. *Astrophys. J.*, **244**, 33.
Ollongren, A., 1962. *Bull. astr. Insts Neth.*, **16**, 241.
Peterson, C. J., 1978. *Astrophys. J.*, **222**, 84.
Schecter, P. L. & Gunn, J., 1979. *Astrophys. J.*, **229**, 472.
Schwarzschild, M., 1979. *Astrophys. J.*, **232**, 236.
Schweizer, F., 1979. *Astrophys. J.*, **233**, 23.
Stark, A. A., 1977. *Astrophys. J.*, **213**, 368.
Strom, K. M. & Strom, S. E., 1978a. *Astr. J.*, **83**, 73.
Strom, K. M. & Strom, S. E., 1978b. *Astr. J.*, **83**, 732.
Strom, K. M. & Strom, S. E., 1978c. *Astr. J.*, **83**, 1239.
Sunyaev, R. A. & Zeldovich, Y. B., 1972. *Astr. Astrophys.*, **20**, 189.
di Tullio, G. A. 1979. *Astr. Astrophys. Suppl.*, **37**, 591.
White, S. D. M., 1978. *Mon. Not. R. astr. Soc.*, **184**, 185.
Williams, T. B. & Schwarzschild, M., 1978. *Astrophys. J.*, **227**, 56.
Young, P. J., Sargent, W. L. W., Boksenberg, A., Lynds, C. R. & Hartwick, F. D. A., 1978. *Astrophys. J.*, **222**, 456.
Young, P. J., Sargent, W. L. W., Kristian, J. & Westphal, J. A., 1979. *Astrophys. J.*, **234**, 76.